Nanosized Zeolite P for Enhanced CO2 Adsorption Kinetics

Jaouad Al Atrach, Abdelhafid Aitblal, Abdallah Amedlous, Ying Xiong, Marie Desmurs, Valérie Ruaux, Rémy Guillet-Nicolas, Valentin Valtchev

Nanosized zeolite P for enhanced CO_2 adsorption kinetics

Jaouad Al Atrach,[a] Abdelhafid Aitblal,[a] Abdallah Amedlous,[a] Ying Xiong,[a] Marie Desmurs,[a] Valérie Ruaux,[a] Rémy Guillet-Nicolas,[a] Valentin Valtchev[a,b*]*

[a] Université de Normandie, ENSICAEN, UNICAEN, CNRS, Laboratoire Catalyse et Spectrochimie (LCS), Caen, 14050, France

[b] University of Sofia, Faculty of Chemistry and Pharmacy, 1126 Sofia, Bulgaria

ABSTRACT

Downsizing zeolite crystals is a rational solution to address the challenge of slow adsorption rates for industrial applications. In this work, we report an environmentally friendly seed-assisted method for synthesizing nanoscale zeolite P, which has been shown to be promising for binary separations.The Potassium-exchanged form of nanoagglomerates demonstrates dramatically enhanced CO_2 adsorption capacity, improved diffusion rate, and separation performance. Single-component CO_2 adsorption at equilibrium demonstrated higher CO_2 uptake and faster adsorption kinetics (ca. 1400 s *vs* >130000 s) for nanosized zeolite (KP1) compared to its micron-sized (KP2) counterpart. The diffusion kinetics analysis revealed the relation between the crystal size and the transport mechanism. The micron-sized KP2 sample was primarily governed by a surface barrier resistance mechanism, while in KP1, the diffusion process involved both intracrystalline and surface barrier resistance, facilitating the surface diffusion process and enhancing the overall diffusion rate. Breakthrough curve analysis confirmed these findings as fast and efficient CO_2/N_2 and CO_2/CH_4 separations recorded for the nanosized sample. The results showed remarkably

enhanced breakthrough time for KP2 *vs* KP1 in CO_2/N_2 (1.0 *vs* 10.9 min) and CO_2/CH_4 (1.1 *vs* 9.9 min) mixtures, along with much higher adsorption capacity for CO_2/N_2 (0.18 *vs* 1.33 mmol/g) and CO_2/CH_4 (0.18 *vs* 1.21 mmol/g) mixtures. The set of experimental data demonstrates the importance of zeolite crystal engineering for improving the gas separation performance of processes involving CO_2, N_2, and CH_4.

Keywords: nanozeolites, seed-assisted synthesis, CO_2 adsorption, adsorption kinetics, CO_2 diffusion, breakthrough analysis

1. Introduction

In light of the ongoing global effort to achieve carbon neutrality, carbon capture and storage (CCS) is a significant technology to reach this goal. Recognized as a key solution to mitigate CO_2 emissions, CCS aligns with the long-term temperature goal (LTTG) established by the Paris Agreement.[1,2] In this context, zeolites, defined as a class of aluminosilicate porous materials, stand out as one of the most widely studied solid adsorbents for CO_2 capture and separation. This is attributed to their crystalline structure, well-defined micropores, adjustable chemical composition, and physicochemical stability.[3] They are considered among the most promising solid-state adsorbents for selectively capturing CO_2 over other small gases such as N_2 and CH_4.[4] In the vast majority of cases, the existing literature solely focuses on factors such as high capacity, high selectivity, and long-term chemical and physical stability when discussing the performance of adsorbents. However, realistic separation processes, such as rapid pressure or vacuum swing adsorption (PSA, VSA) and temperature swing adsorption (TSA), require adsorbents with fast CO_2 diffusion rates. Conventional zeolites with a micrometer particle size pose a challenge for CO_2 molecules, requiring them to “travel” a substantial tortuous distance through the pores to find a potential adsorption site. This issue can be mitigated by introducing

mesoporosity or reducing the particle size, thus enhancing molecular access to zeolite micropores. However, introducing mesoporosity that will synergically interconnect with the existing microporosity without altering the other properties of zeolites is not trivial, and leads to the use of costly reactants and several post-synthesis steps of treatment. It results in longer and more complex production times, increased costs, and larger resource consumption.[5] Therefore, synthesizing zeolites with nanoscale dimensions would significantly decrease the diffusion distance for guest molecules within the particles, offering easier and more direct accessibility, larger surface areas, and more available active sites.[6,7] The regulation of zeolite crystal size and shape improves diffusion and enhances the sorbent's kinetic selectivity.[8]

Various methods for synthesizing nanozeolites have been proposed, including the use of structure-directing agents (OSDAs) and other synthesis modifiers to control the crystal size. However, employing organic templates for nanozeolite synthesis entails significant drawbacks, including high costs, toxicity linked to organic templates, and the need for post-synthetic calcination, which can compromise zeolite structural integrity and contribute to increased energy consumption and CO_2 emissions.[9] Consequently, alternative techniques have emerged to address these challenges, such as recycling unused chemicals,[10] ionothermal synthesis,[11] microwave and sonication-based approaches,[12] and seed-assisted methods.[13,14] Traditionally, seed-assisted synthesis has played a crucial role in reducing zeolite synthesis time. Recently, several studies have reported that an ultrafast synthesis route using seeds has enabled the rapid preparation of a variety of industrially vital zeolites, including ZSM-5[15] and SSZ-13,[16] often within hours or even minutes.[17–19] Moreover, it is well established that using seeds in zeolite synthesis improves the crystallization kinetics, suppresses impurity formation and, as mentioned, enables precise control of particle size and morphology.[13,20,21] Recent advancements in seed-assisted approaches have

revolutionized zeolite synthesis, reducing or eliminating the need for OSDAs, thus opening new frontiers in zeolite production.[22,23]

A small-pore zeolite P has a gismondine (GIS) type framework topology with two intersecting channels of 0.31 × 0.44 nm and 0.26 × 0.49 nm in [1 0 0] and [0 1 0] directions, respectively.[24] McCusker et al. illustrated that the GIS-type framework could be characterized as a stacking arrangement of two-dimensional arrays of double crankshaft chains (dccs).[25] This structural feature contributes to the framework flexibility, leading to the observation of various symmetries in GIS types. Recently, researchers have identified the crystallization of GIS-type frameworks in more than 20 distinct space group symmetries.[26] The GIS framework distortion yields two isotypes, P1 and P2, each presenting different pore sizes and shapes. In P1 crystals, all dccs align uniformly in one direction. Conversely, P2 crystals feature alternating dccs with a slight misalignment of ± 15° rotation. This slight orientation shift of dccs leads to a narrower 8-MR pore aperture in P2 compared to P1, despite the overall similarity in pore network structures.[27] Due to the difficulty in distinguishing between the P1 and P2 phases, this zeolite is often referred to the scientific literature as'zeolite P' without clear differentiation. The micropore size of GIS-NaP1 zeolite is smaller than those of MFI, FAU, MOR, and BEA zeolite types. This unique feature makes zeolite P particularly well-suited for separating very small gases. Indeed, some theoretical studies have identified zeolite P as one of the most promising zeolite adsorbents for this purpose.[28] Force field simulations employing an all-silica model reinforced this perspective by highlighting the GIS structure as the optimal choice for CO_2 adsorption, aiming for efficient CO_2/N_2 separation.[29]

Zeolite P was initially discovered as an impurity during zeolite synthesis in sodium-rich, highly alkaline aluminosilicate gels using only inorganic components.[30] Zeolite P synthesis typically

takes less than a week. However, the well-known verified International Zeolite Association (IZA) recipe involves a lengthy 60-day process.[31] This extended duration is likely due to the use of lower hydrothermal temperature treatment at 85 °C and a NaF-rich medium. Regarding the nanosized version of zeolite P, it was first prepared from an aged aluminosilicate precursor solution containing tetramethylammonium (TMA) hydroxide, yielding crystalline GIS particles with a hydrodynamic radius ranging from 30 to 50 nm.[32] Recently, Zare et al. reported the hydrothermal synthesis of nanocrystalline zeolite P using 1-dodecyl-3-methylimidazolium chloride ([C_{12}mim][Cl]) ionic liquid as a template.[33] The resultant zeolite P exhibited a high surface area with a crystal size exceeding 30 nm. In addition to the conventional hydrothermal method, nanoparticle synthesis of zeolite P was also conducted via a microwave-assisted method for 1 h, resulting in crystals with a high adsorption capacity for Mn^{2+} ions in aqueous media.[34]

Herein, we present a free-template synthesis of highly pure nanocrystalline P zeolite using a relatively small amount of seeds, lower temperatures, and a shorter synthesis time. To better understand the changes in isotype, particle size, and shape that occur during the crystallization process, several techniques were employed, including X-ray diffraction (XRD), scanning electron microscopy (SEM), and energy dispersive (EDS) analysis. The potency of the synthesized P nanozeolites for CO_2 adsorption and separation was tested, and its performance was compared to its micron-sized analog using equilibrated single-component adsorption measurements. Furthermore, adsorption kinetics in both samples were investigated to understand their adsorption-diffusion mechanisms better. Dynamic adsorption measurements performed through breakthrough curve analysis validated the enhanced diffusion properties of the nanosized adsorbent and their relevant CO_2 separation performance. With the ongoing sustainability issues,

our results demonstrate the importance of rationalized zeolite crystal engineering using greener, cheaper, and energy-efficient alternatives to improve important industrial processes' performance.

2. Experimental Section

Materials

Sodium hydroxide solution (NaOH, Thermo scientific, 50 wt% suspension, 99.5%), sodium aluminate ($NaAlO_2$, Al_2O_3 50–56 wt. %, Na_2O 40–45 wt.%, Sigma-Aldrich), sodium silicate (SiO_2 25%, Na_2O 8.06%, H_2O 66.94%, Sigma-Aldrich, 99.9%), and potassium nitrate (KNO_3 Thermo scientific, 99.5%) were used as received. Water was deionized using an Aquatron water still A4000D.

Synthesis

Synthesis of NaP2 seed parent: NaP2 zeolite was prepared with a gel composition of 4.5 Na_2O: 1 Al_2O_3: 10 SiO_2: 180 H_2O. In a typical synthesis, sodium aluminate, sodium hydroxide solution, and deionized water were mixed in a polypropylene bottle and stirred at room temperature for 15 min until a clear solution was obtained, and then a solution of sodium silicate was added dropwise with vigorous stirring. The resultant mixture was aged at room temperature for 24 h, then transferred to a Teflon-lined autoclave and heated in a static oven at 120 °C for 24 h. Finally, the sample was recovered by centrifugation at 20,000 rpm for 20 min, washed with deionized water (4 times), and dried overnight at 60 °C.

Synthesis of NaP1: the synthesis procedure for NaP2 was repeated with the same gel composition, and preformed NaP2 crystals were introduced as seeds (3% relative to SiO_2). In this case, the mixture was aged for 30 min, and seeds were added 10 min prior to hydrothermal treatment. The mixture was then heated at 100 °C for 24 h. The synthesis was repeated under the

same conditions, but using the synthesized NaP1 as a seed to produce the second generation of NaP1 (2^{nd} Gen).

During the seed-assisted synthesis process, the synthesis time, ranging from 1 to 24 h, and temperature, ranging from 60 to 140 °C, were systematically varied to study their effects on the synthesis of GIS zeolite.

Ion Exchange

1.0 g of the obtained NaP2 and NaP1 samples were introduced into 50 mL of a potassium nitrate (KNO_3) solution with 1 M concentration for ion exchange. These mixtures were stirred using a magnetic stirrer at 80 °C for 3 h. The exchange process was repeated twice to ensure the complete replacement of Na cations with K cations. Afterward, the resulting samples were centrifuged at 20,000 rpm for 20 min, washed with deionized water 4 times, and then dried at 60 °C overnight.

General Characterization

Powder X-ray diffraction data were recorded using a PANalytical X'Pert Pro diffractometer with CuKα1 radiation (λ = 1.5406 Å, 45 kV, 40 mA). The samples were scanned from 5 to 50 ° (2 theta) with a step size of 0.0167113 and a time per step of 1200 s. Scanning electron microscopy (SEM) images of the zeolite samples were obtained using FE-SEM (JSM-IT800SHL, JEOL) operated at an acceleration voltage of 0.3 kV. The elemental composition was assessed using energy dispersive X-ray spectrometry (EDS) by combining EDS detectors with FE-SEM, and analyses were performed at 5 kV accelerating voltage and 700 pA probe current with an acquiring time of 2 min. Prior to measurements, samples were prepared by depositing < 1 mg of the powder on specimen holders using double-sided sticky tape. Chemical analysis of samples was performed through inductively-coupled plasma mass spectrometry (ICP-MS) using 7900

ICP-MS from Agilent technologies. Thermogravimetric analysis (TG-DTG) was performed using the STA 449 F5 Jupiter instrument. The analysis was conducted in a nitrogen flow environment over a temperature range of 30 to 800 °C, with a constant flow rate of 40 mL/min and a heating rate of 5 °C/min. ^{27} Al and ^{29} Si MAS NMR experiments were conducted using a Bruker AVANCE 500 NB spectrometer operating at a rotational speed of 12 kHz. For ^{27} Al MAS NMR, the experiment was performed at 130.30 MHz with a 3.2 mm probe head, using $Al(NO_3)_3$ as a reference for the chemical shift. In the case of ^{29} Si MAS NMR, experiments were carried out at 99.35 MHz with the same 4 mm probe head. TMS was used as the reference for the chemical shift.

Equilibrium Adsorption Measurements

Single-Component Gas Adsorption Measurements

Nitrogen adsorption−desorption isotherms were measured at −196 °C, using a Micromeritics 3Flex high-resolution surface characterization analyzer unit. Additionally, physisorption isotherms of CO_2, N_2, and CH_4 at 25 °C in the pressure range of 0–1.0 bar were obtained with a Micromeritics ASAP2020 instrument. Before the measurement, approximately 100 mg of the sample underwent degassing at 250 °C under vacuum for at least 6 h.

CO_2 adsorption kinetic measurements were conducted at 25 °C using an iSorb HP Quantachrome instrument. Samples were outgassed according to the same conditions described above. The rate of adsorption in the iSorb HP software reports the amount adsorbed at 0.05 bar with time ranging from 1 to 130,000 s. Adsorption kinetic curves were fitted using equations governed by surface barrier resistance and intracrystalline diffusion,[35] respectively:

Intracrystalline diffusion model: $$\frac{Q_t}{Q_{\max}} = 1 - \frac{6}{\pi^2}\sum_{n=1}^{\infty}\frac{1}{n^2}\exp\left(-\frac{n^2\pi^2 D_e}{r^2}t\right) \quad \textbf{Eq. 1}$$

Surface barrier resistance model: $$\frac{Q_t}{Q_{\max}} = 1 - \exp\left(-\alpha \frac{3}{r} t\right)$$ **Eq. 2**

Where Q_t/ Q_{max} is the fractional uptake, i.e. the ratio of Q_t, the total amount adsorbed after time t to Q_{max}, the total amount adsorbed at equilibrium, D_e is the effective diffusivity, r is the radius of the crystallites, and α is the surface permeability.

Dynamic breakthrough adsorption measurements

Breakthrough measurements were carried out at 25 °C using a 3P instrument SHP eco equipped with a Cirrus-3 quadrupole mass spectrometer, following established procedures as detailed in previous work.[36] The zeolite samples were prepared as pellets by loading powder between two core dices in a 20 mm die sleeve with a base plate and plunger and increasing the applied pressure to ~1.5 tonnes. The pellets were crushed and sieved into the desired fraction of 250–500 µm. The prepared zeolite samples were loaded into a 6 mm column and subjected to a gradual heating process for activation at a rate of 10 °C/min until reaching 300 °C, where they were held for 9 h under helium flow (20 mL·min^{-1}). Prior to activation, TG analysis was conducted to measure the weight loss of water throughout the activation process. Once activated, the column contained 0.686 g of KP2 and 0.536 g of KP1. The zeolite samples were maintained under helium flow (20 mL·min^{-1}) at 25 °C before starting the breakthrough measurements.

Two calibrated ternary gas mixtures, CO_2, N_2, and He, for the first case, and CO_2, CH_4, and He, for the second case, were used in breakthrough curve measurements. The experiments were conducted under a pressure of 1 bar, with He as the carrier gas. Using a bypass line, the ternary mixtures were calibrated through the mass spectrometer. Once the stability of both temperature and spectrometer signals was achieved, the gas stream within the column was switched from pure He to the specified feed mixture. Following a predetermined period to achieve saturation of the

adsorbent bed (60 and 30 min for the CO_2/N_2/He and CO_2/CH_4/He mixtures, respectively), a desorption step was initiated by switching the feed composition back to 100% He. The desorption flow rates were set at 40 mL·min^{-1} for CO_2/N_2 separation experiments and 20 mL·min^{-1} for CO_2/CH_4 separation experiments. With a pressure sensor positioned immediately before the column and another located just after it, the pressure drop across the loaded column was observed. Throughout all experiments, the observed pressure drops were consistently below 0.07 bar or 6% of the column pressure.

The calculation process for the adsorbed amounts was processed using the MixSorb Manager software.

$$n_{\text{adsorbed}} = \int V_{\text{in}}(t) c_{\text{in}}(t) dt - \int V_{\text{out}}(t) c_{\text{out}}(t) dt \quad \textbf{Eq. 3}$$

The computed alterations in flow rates were used to account for changes in the flow rate using the He carrier gas as an internal standard.

$$V_{\text{out}}(t) = \frac{V_{\text{He}}(t)}{1 - \sum_{i=1}^{n} y_{\text{adsorptive},i}(t)} \quad \textbf{Eq. 4}$$

Blank breakthrough curves under matching conditions (gas mixture composition, temperature, and flow rate) were measured on granular quartz (200–800 µm) to quantify the adsorbed amounts in the void spaces between the adsorbent particles. The calculated loadings from the granular quartz were then subtracted from the values obtained for the zeolite samples, while considering the mass of the adsorbent.

The calculated CO_2/N_2 (15:85, v/v) and CO_2/CH_4 (40:60, v/v) selectivities for both equilibrium and dynamic experiments were calculated using the following equation:

$$S_{ads} = (q_i/q_j)/(p_i/p_j) \quad \textbf{Eq. 5}$$

In this equation, q_i and q_j are the equilibrium molar uptakes of components i and j, while p_i and p_j are the partial pressure of the latter components.

3. Results and Discussion

X-ray Diffraction Studies

Figure 1 a presents XRD patterns of samples crystallized at 120 °C for 6, 12, and 24 h. The 6 h sample shows typical NaX peaks, whereas the one crystallized for 12 h exhibits FAU- and GIS-type peaks. However, after 24 h, only NaP2 peaks were detected, confirming a classical crystallization process involving interzeolite transformations (IZTs) from FAU to GIS types. Generally, the ability of various zeolite types to crystallize simultaneously or consecutively depends on the chemical composition of the crystallizing system and the synthesis conditions. The order of appearance and yields of different zeolite types in the reaction mixture are determined by the relative thermodynamic stabilities of the co-crystallized zeolite phases.[37] In this case, the NaX zeolite of the FAU type is in the metastable phase, being fully transformed into NaP2 after 24 h of hydrothermal treatment.

In contrast to the conventional synthesis, the seed-assisted one performed at 100 °C led to the crystallization of NaP1 GIS-type zeolite, as depicted in Figure 1 b. The similarity between the thus obtained XRD patterns was confirmed using simulated NaP1 from the IZA structure database as a reference. This effect is attributed to the complete transformation of the less stable phase NaP2 into the most stable NaP1 one. Similar behavior has already been reported in the literature by Subotic et al., who studied the structural transformation from NaP2 to NaP1.[38,39] They observed that the NaP2 zeolite initially appeared as the first crystalline phase and gradually

transformed into NaP1 over extended reaction times. Therefore, it is evident that the presence of NaP2 crystal seeds in the system accelerates nucleation kinetics and alters the course of interzeolite transformations (IZTs) from NaX-to-NaP2 to NaP2-to-NaP1, resulting in a pure NaP1 phase after only 24 h at 100 °C. Replacing NaP2 seed crystals with NaP1 seeds in the seed-assisted synthesis of zeolite P resulted in NaP1 (2^{nd} Gen) phase formation, as shown in Figure 1 b, indicating that the used NaP seed type has no influence.

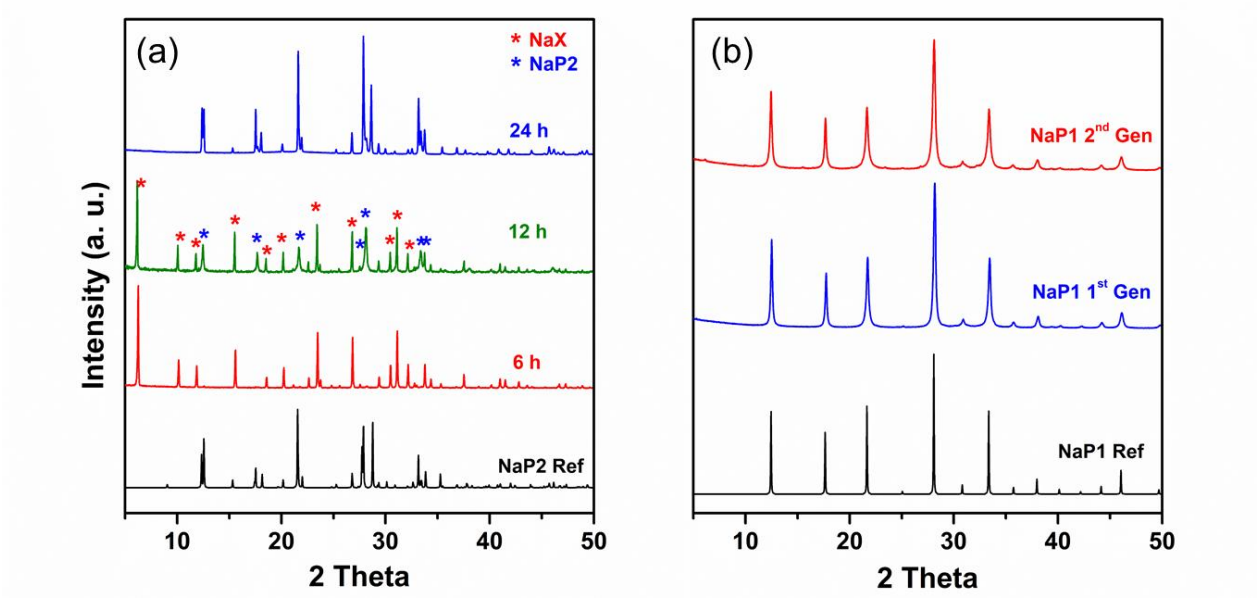

Figure 1: XRD patterns of (a) simulated NaP2 from the IZA structure database and as-synthesized NaP2 heated for different synthesis times: 6, 12, and 24 h at 120 °C. (b) Simulated NaP1 from the IZA structure database and as-synthesized NaP1 1^{st} and 2^{nd} Gen at 100 °C for 24 h.

XRD analysis of as-prepared samples from the synthesis carried out at 100 °C and different crystallization times (Figure S1) showed that the amorphous solid phase begins to transform into the crystalline phase NaP2 after only 1 h of hydrothermal treatment, followed by a complete transformation into NaP1 after 4 h. Increasing the synthesis time to 8 and 24 h had a positive impact on the crystallinity of NaP1, reaching 85% crystallinity after 8 h of hydrothermal treatment. To the best of our knowledge, the previous fastest conventional hydrothermal

synthesis of single-phase GIS-P1 at 100 °C was reported by Sharma et al. and involved a 24 h aging followed by 24 h synthesis.[40] Therefore, the proposed seed-assisted synthesis method is the fastest protocol ever reported for obtaining pure NaP1 zeolites through conventional hydrothermal treatment.

The impact of the synthesis temperature on the seed-assisted procedure was also investigated by fixing the synthesis time at 24 h. As observed in the resulting XRD patterns (Figure S2), when the synthesis was conducted below 60 °C, the formation of zeolite P1 crystals was not fully completed, and evidence of an amorphous phase was detected in the XRD pattern. This suggests that there is not enough energy at this temperature to fuel the complete transformation of the precursor aluminosilicate gel into NaP1 crystals. Consequently, only a portion of the aluminosilicate gel was transformed into NaP1 crystals. Raising the temperature between 80 and 120 °C was clearly beneficial, as indicated by the XRD results, which all displayed a pure NaP1 phase with no additional peaks up to 120 °C, after which a very minor impurity of the ANA zeolite started to appear. However, with a further increase in the temperature to 140 °C, the GIS material was entirely transformed into the denser analcime (ANA-type) zeolite. Therefore, the optimal conditions for highly crystalline GIS-NaP1 synthesis were determined to be 100 °C for 24 h. The results discussed above highlight the effectiveness of seed-assisted synthesis in reducing both the synthesis time and temperature for effective zeolite P preparation.

Impact of Seeds on Crystal Size and Morphology

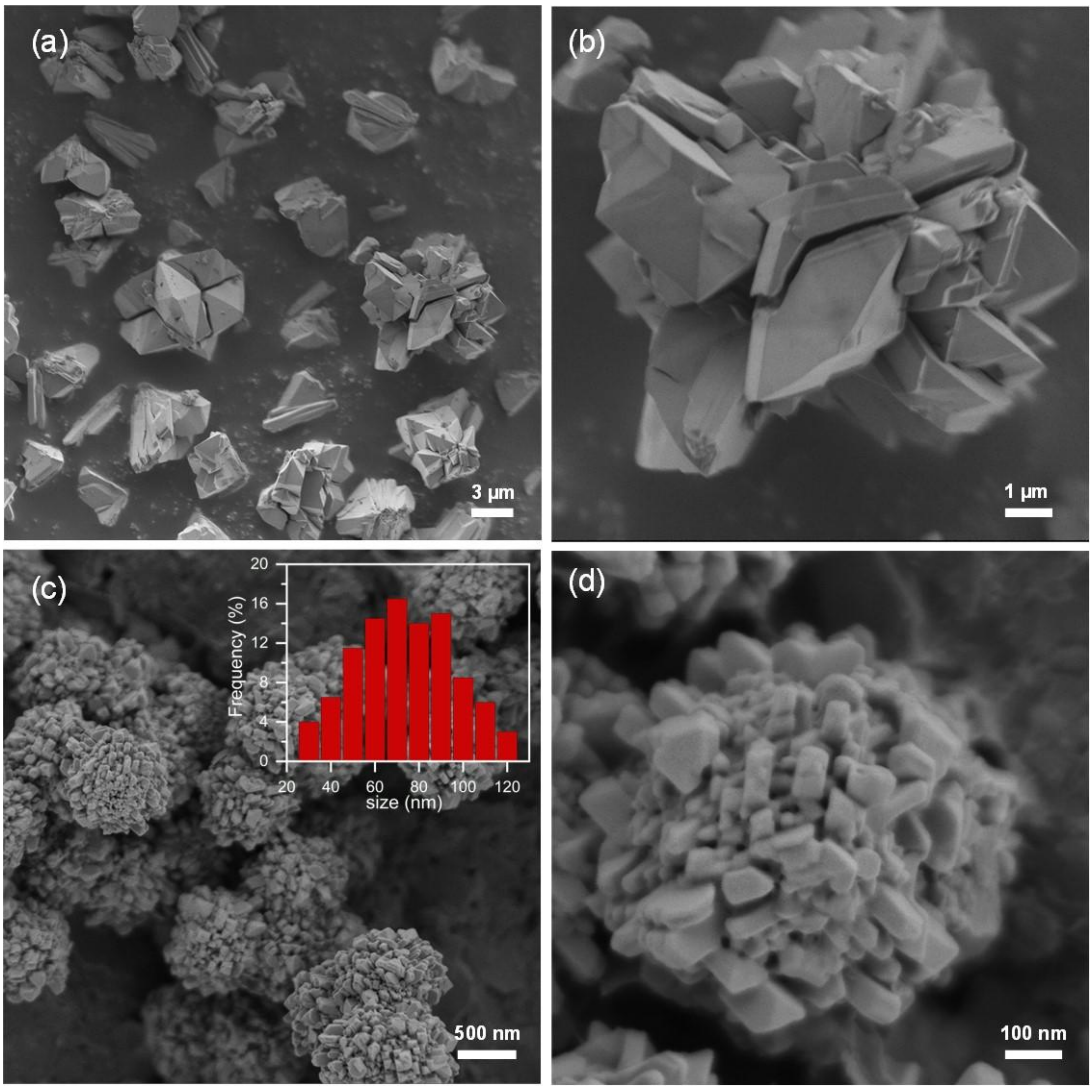

Figure 2: SEM images of NaP2 (a, b) and NaP1 (c, d) zeolite samples with crystal size distribution of NaP1.

The utilization of seeds in zeolite synthesis is known to yield products with significantly altered crystal size and shape compared to those derived from classical synthesis. We thus investigated the influence of "seeding" on crystal size and morphology. When NaP2 synthesis was carried out without using seeds, diamond-like crystals were formed with distinct edges, confirming their high crystallinity (Figure 2 a, b). Each diamond had a size rang of 5−10 µm. In contrast, when seeds were added to the same synthesis protocol, the resulting NaP1 zeolite exhibited agglomerates of

spherical shape (Figure 2 c, d). The individual particle size was approximately 30–120 nm, while the particle clusters were about 500–800 nm in size. When NaP1 zeolite products were used as seeds to synthesize NaP1 (2^{nd} Gen), the resulting crystals retained the same morphology and individual crystal size as the seeds, while the particle clusters decreased to 300–500 nm in size (Figure S3).

The mechanism of nanozeolite crystal formation using the seed-assisted approach is not fully understood and the active species promoting growth in a seeded zeolite system remain unclear.[41] However, some guidelines could be proposed to explain the relationship between NaP2 seeds and the resulting NaP1 product. Based on the varied crystal sizes and shapes of the NaP1 nanocrystal product (Figure 2 c), it is more likely that the micron-sized NaP2 seeds partially dissolve during the synthesis process, leading to heterogeneous nucleation. It is known that heterogeneous nucleation might result in faster growth due to multiple nucleation sites. In this process, the NaP2 seeds act as nucleation sites, bypassing the slow nucleation stage and directly promoting crystal growth, which accelerates the overall crystallization process and leads to the formation of NaP1 nanoaggregates. This intriguing mechanism warrants further investigation; however, it is not the main focus of this study, which aims to investigate the enhanced adsorption properties of nanocrystal NaP1.

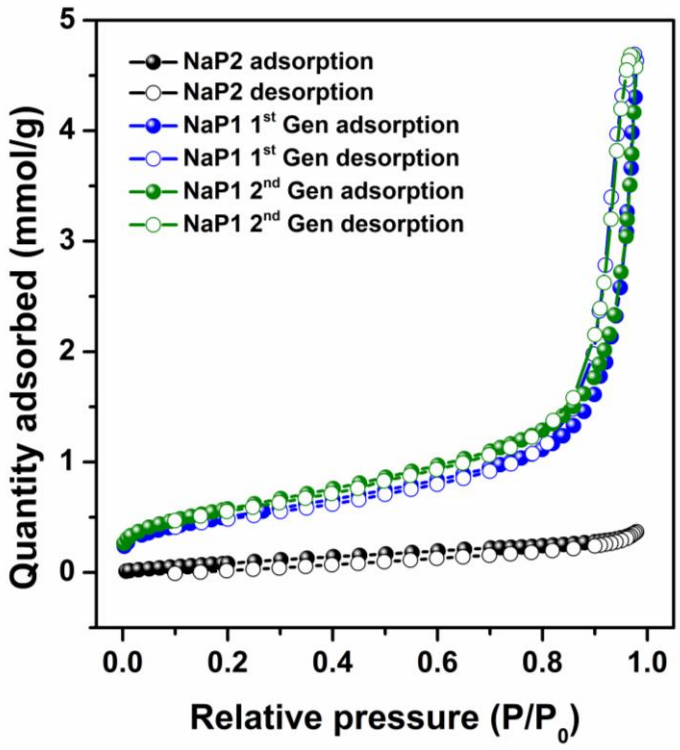

Figure 3: N_2 adsorption-desorption isotherms of NaP2, NaP1 (1st Gen) and NaP1 (2nd Gen) at – 196 °C.

Figure 3 illustrates N_2 adsorption−desorption isotherms measured at –196 °C. Textural properties, together with the chemical composition of zeolites, are summarized in Table S1. These data reveal that NaP1 zeolite obtained by the seed-assisted synthesis exhibits textural mesoporosity. For instance, NaP1 possesses a mesopore volume of 0.16 cm^3/g, which is approximately 16 times larger than the value (0.01 cm^3/g) of microcrystalline NaP2, suggesting significant textural porosity. The mesopore volume of NaP1 (2nd Gen) was found to be identical to that of NaP1, indicating no further increase in textural mesoporosity. The BET specific surface areas of the samples, as calculated from N_2 isotherms at – 196 °C, show that NaP1 (1st Gen) exhibits the highest BET surface area at 45 m^2/g, followed by NaP1 (2nd Gen) at 43 m^2/g, both of which are substantially higher than NaP2 zeolite at 9.6 m^2/g.

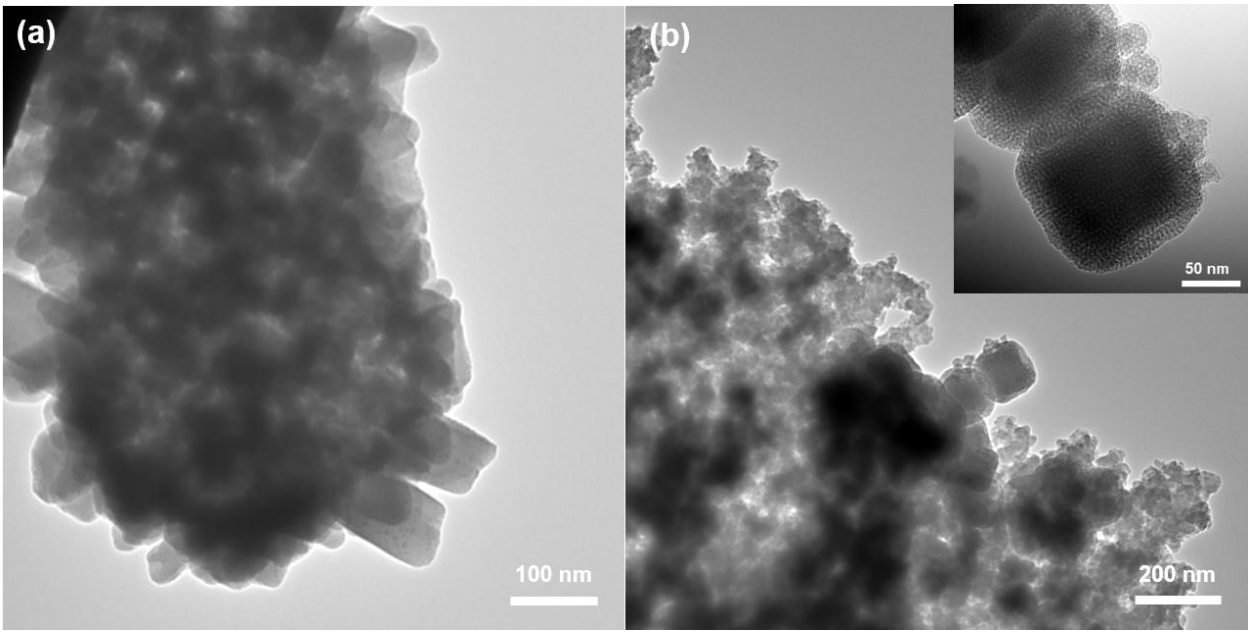

Figure 4: TEM images at low (a) and high (b) magnifications for the NaP1 zeolite with two different magnifications.

In line with SEM and physisorption observations, TEM images at low magnification (Figures 4a andS4) elucidate the nanoscale morphology of the NaP1 sample, revealing that each particle cluster is composed of numerous closely packed nanocrystals with polyhedral-like shapes and inhomogeneous sizes, consistent with the sizes observed by SEM analysis. The TEM micrograph at higher magnification (Figure 4 b) further confirms the textural nature of the mesopores probed through N_2 physisorption experiments. Indeed, one can clearly see the assembly of nanocrystals, creating mesoporous interstices between them.

The ^{27} Al MAS NMR spectroscopic analysis of both NaP2 and NaP1 samples, as shown in Figure S5, reveals a single resonance at 58.5 ppm, indicating aluminum atoms in a tetrahedral coordination environment within the framework. No peaks were observed at 0 ppm, suggesting the complete incorporation of aluminum atoms into the P zeolites. In the ^{29} Si MAS NMR spectra, five resonances at −87, −91, −96, −102, and −107 ppm were observed, corresponding to Si(nAl)

coordination, where n equals 4, 3, 2, 1, and 0, respectively (Table S2). Deconvolution and analysis of the ^{29}Si MAS NMR spectra yield framework Si/Al ratios of 1.50 and 1.7 for NaP2 and NaP1, respectively, consistent with the Si/Al ratio determined from EDS and ICP-MS experiments (Table S3). The TG-dTG curves presented in Figure S6 revealed distinctive weight loss profiles for NaP2 and NaP1 samples. In the 30−350 °C temperature range, NaP2 exhibits a 14.8 wt.% water loss, characterized by three distinct mass loss steps corresponding to the removal of adsorbed water on the surface, in GIS channels, and hydroxyl groups, respectively. Conversely, NaP1 samples display a 16.0−16.5 wt. % water loss within the same temperature range, featuring two mass loss steps associated with the removal of adsorbed water in GIS channels and intraparticle mesopores, as well as the elimination of hydroxyl groups. The observed variations in TG curve shapes and weight loss are attributed to the differences in particle morphologies.

CO_2 Adsorption and Separation Performance

In line with previous literature findings,[27] the CO_2 adsorption capacity of standard zeolite P materials is relatively low (Figure S7). At 25 °C and 1 bar, the recorded adsorption capacity was 0.12 and 0.26 mmol/g for NaP2 and NaP1, respectively. This reduced capacity was primarily influenced by the strong "cation-gating" effect that fully blocks the 8MR windows.[42] To address this challenge, we substituted Na^+ cations with K^+ ones, a larger counterion with higher charge density that could influence the zeolite framework's basicity, flexibility, and mobility. The resulting PXRD patterns exhibited slight peak shifting and splitting, confirming the successful insertion of K^+ cations into the zeolite P pore network (Figure S8). Elemental analysis and EDS further validated the complete ion exchange (Table S4).

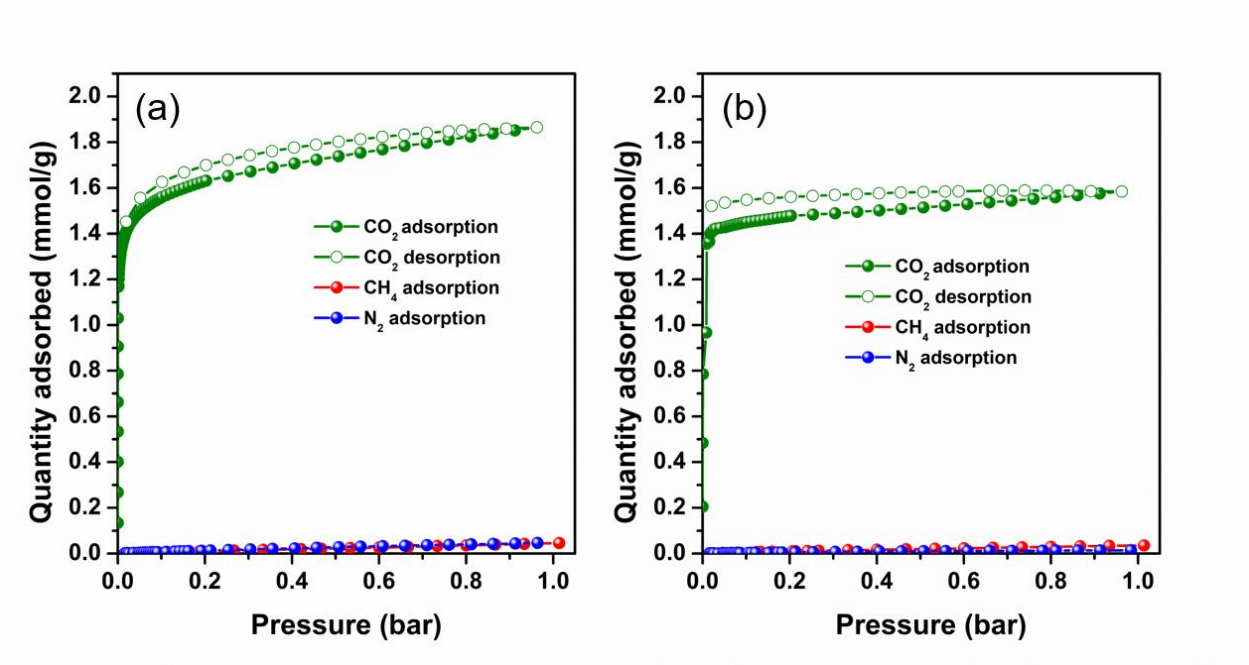

Figure 5: CO_2, N_2, and CH_4 adsorption-desorption isotherms of KP1 (a) and KP2 (b) at 25 °C and 1 bar.

Contrary to sodium-form, the K-exchanged zeolites exhibit high CO_2 uptake, reaching 1.6 and 1.9 mmol/g for KP2 and KP1, respectively (Figure 5a and b). These uptakes are respectively 8 and 13 8 times higher than those observed for the sodium-form zeolites. The introduction of larger basic cations, such as potassium, thus led to a substantial increase in the CO_2 uptake. This behavior can be rationalized considering the flexible pores of zeolite P, in which micropore space becomes accessible as a result of K^+ cation displacement within the pores. Similar adsorption behavior has already been reported for low silica and small-pore flexible zeolites such as PHI and MER.[43,44] K-PHI and K-MER with Si/Al ratios of 2.5 and 2.3, respectively, showed higher CO_2 uptake over other alkali-exchanged counterparts. The process of CO_2 adsorption is believed to occur through the "trapdoor" mechanism, wherein cations temporarily shift away from the pore window.[45] The cations' thermal motion and interactions with CO_2 molecules are determined by the pore opening size, cation radius, and polarizability.[46] Similar to PHI and MER zeolites, CO_2

adsorption on the K-exchanged zeolite samples is enabled thanks to this “trapdoor” type cation gating mechanism.

Both samples exhibited negligible uptakes of the weak components N_2 and CH_4, resulting in extremely high CO_2 ideal selectivity: 619 and 215 over N_2 and 97 and 96 over CH_4 for KP2 and KP1, respectively (Table 1). The enhanced selectivities can be attributed to the small pore diameter and high surface polarity of K-GIS materials. This high selectivity also arises because CO_2 efficiently induces the temporary migration of K^+ cations from the center of 8MRs, facilitating the entry of CO_2 molecules into GIS-type zeolite pores, a process not accessible for N_2 and CH_4 (molecular trapdoor effect). KP2 exhibited significantly higher CO_2/N_2 selectivity as compared to KP1 most likely due to its lower external surface area limiting the adsorption of N_2 (Table S5 and Figure S9). Although the adsorption capacity of CO_2 for K−P samples is lower than that of other porous materials (Table 1), N_2 adsorption for both K−P materials remains almost negligible. Thus, the selectivity for KP2 was found to be higher than some of the best-performing zeolites and metal−organic frameworks, and comparable to the highly selective zeolite NaKA (17% K^+) with a value of 660 at 0 °C. [47] This data was obtained from static equilibrium sorption experiments. It is important to note that while such comparisons do not account for significant real-world applications such as accessibility and diffusion dynamics, they still provide a crucial preliminary insights into the material’s potential behavior and properties. In the upcoming sections, we will focus on diffusion dynamics by analyzing CO_2 adsorption kinetics and dynamic breakthrough measurements to establish the true potential of K−P material clearly.

393

394 Table 1: Adsorption Capacity and CO_2 Selectivity for Different Types of Porous Materials at 1

395 bar and 25°C.[a]

Material	nCO_2 (mmol/g)	nN_2 (mmol/g)	nCH_4 (mmol/g)	CO_2/N_2	CO_2/CH_4	ref
silicate-1	1.83	0.20	0.66	15	4	[48]
LTA-5 [b]	5.15		1.4		24	[49]
13X [b]	4.65	0.25	0.43	64	17	[50]
ZSM-5	1.84	0.18	0.8	31	3	[51]
Na-PST-29	4.70	0.57	0.63	37	18	[52]
K-MER	2.9	0.24	0.26	64	28	[53]
SAPO-34	2.39		0.46		7	[54]
Na-SAPO-RHO	3.53	0.08		196		[55]
Na-GIS	3.64	0.18	0.12	75	69	[56]
2K-SSZ-13	4.80	0.47		50		[57]
NaKA [c]	3.40	0.02		660		[47]
activated Carbon	2.04	0.28	0.89	15	3	[58]
UIO-66	1.30	0.15		17	63	[59]
Zn-MOF-74	4.31	0.13	0.51	76	15	[60]
Ni-MOF-74	4.72	0.54	0.39	32	27	[60]
USTA-280	3.04		0.22		41	[61]
ZIF-8	0.81	0.10	0.24	8	3	[58]
KP2	1.58	0.014	0.035	619	97	This work
KP1	1.86	0.046	0.046	215	96	This work

396 [a] Equilibrium selectivity of CO_2/N_2 (15/85, v/v) and CO_2/CH_4 (40/60, v/v) was modeled from the
397 pure component adsorption isotherms.

398 [b] At 30 °C

[c] At 0 °C

Adsorption Kinetics

Figure 6 illustrates the fractional uptake curves of CO_2 at 25 °C and P = 0.05 bar for KP1 and KP2. The time needed for KP1 to reach equilibrium is much shorter than that of KP2, with a steeper curve indicating a faster and more uniform CO_2 diffusion through the particles. For KP2, the fractional approach to equilibrium exhibits a slow increase with time which can be ascribed to the larger particle size and thus longer diffusion path length. The adsorption equilibrium time is reduced from approximately 130,000 s in the case of KP2 to 1400 s in the case of KP1 (Figure S10). These results demonstrate that the adsorption rate can be drastically enhanced for K-exchanged samples by simply decreasing the crystal size.

Several studies have explored the adsorption kinetics in porous materials, offering diverse perspectives on the diffusion and sorbate uptake processes. In zeolites, the dominant mechanisms of gas diffusion are typically identified as surface barrier resistance and intracrystalline diffusion.[35] By analyzing the relationship between the fractional uptake (Q_t/Q_{max}) of CO_2 and the exposure duration to CO_2, the application of eqs 1 and 2 allows for the distinction between these mass transfer mechanisms. This approach is based on the time dependence of the adsorption profiles, providing insights into the dominating diffusion mechanism in K-exchanged samples.

The fitting results indicate that the fractional uptake curve of KP1 closely aligns with both eqs 1 and 2, with a stronger correlation observed with eq 1, especially within the first 40 seconds (Figure 5a). This result suggests that the controlling factors in the CO_2 diffusion mechanism of nanosized KP1 are the surface barrier resistance and intracrystalline diffusion, with a dominance of the intracrystalline diffusion mechanism. On the other hand, for micron-sized KP2, only eq 2 fits well with the fractional uptake curve, indicating that surface barrier resistance predominantly

governs the diffusion process in this sample (Figure 5 b). Table 2 presents the fitting results, showing that D_e/L^2 of K-exchanged samples ranges from 1.31×10^{-4} to 4.36×10^{-2} (s^{-1}) as the size decreases from micron to nanoscale. Simultaneously, a significant improvement in $3\alpha/r$ can be seen from 2.58×10^{-5} in KP2 to 7.79×10^{-4} in KP1, demonstrating that the nanoscale facilitates the surface diffusion process. This enhanced diffusion rate is attributed to the agglomeration of nanozeolite crystals forming a multi-dimensional pore structure of macro-mesopores, which ultimately reduces the diffusion resistance of CO_2 molecules compared to micropores. A comparable trend was observed in the diffusion kinetics of nanosized FAU compared to its micronsized FAU counterpart.[62] This suggests that the improved diffusion properties of nanozeolites can be ascribed to their particle size, i.e., shorter diffusion path length and increased exposure to pore openings.

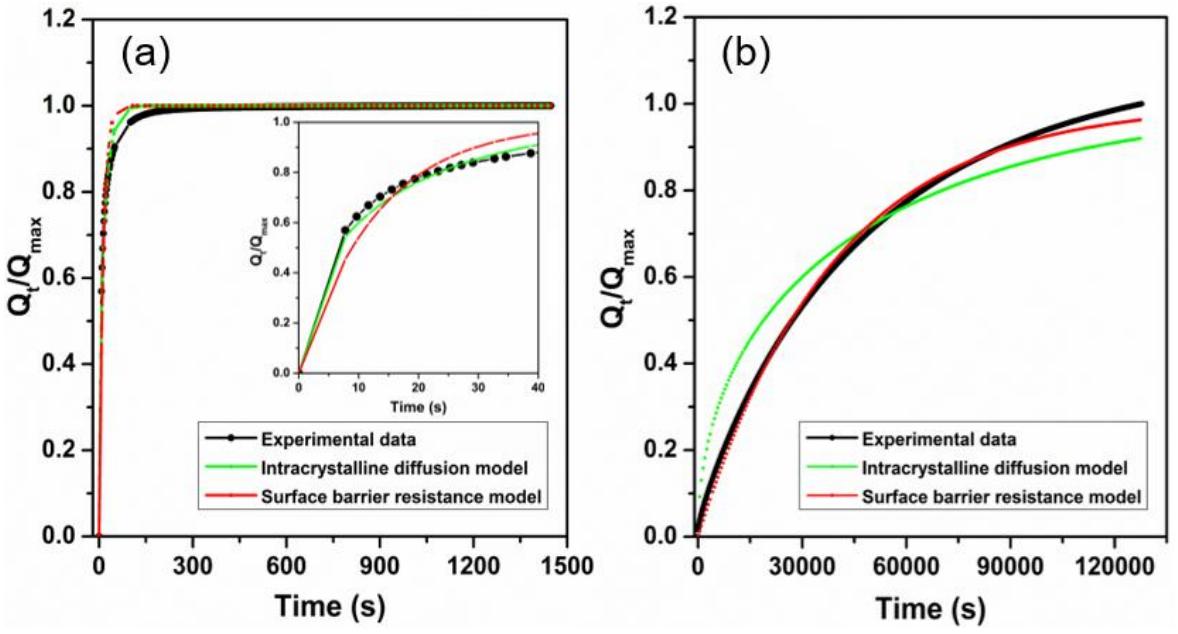

Figure 6: Fractional uptake curves and the fitting results of intracrystalline diffusion and surface barrier resistance models for KP1 (a) and KP2 (b) samples at 0.05 bar and 25 °C.

Table 2: CO_2 Kinetic Adsorption Curves Fitting Results.

Sample	D_e/L^2 (s^{-1})	R^2	$3\alpha/r$ (s^{-1})	R^2
KP1	4.36×10^{-2}	0.9886	7.79×10^{-4}	0.9424
KP2	1.31×10^{-4}	0.9281	2.58×10^{-5}	0.9952

438

439 **Dynamic Breakthrough Experiments**

440 Dynamic breakthrough measurements were conducted on both K-exchanged samples to assess
441 their separation performance under dynamic conditions. The analysis involved $He/N_2/CO_2$
442 (70/25/5 vol %) and $He/CH_4/CO_2$ (75/15/10 vol %) ternary mixtures at 1 bar and 25 °C,
443 simulating conditions representative of pre-purified flue gas and biogas (Figure 6 a, b).
444 Consistent with the equilibrium adsorption results, the weak components, N_2 and CH_4, exhibited
445 instantaneous breakthrough during the adsorption step of ternary mixtures for KP2 and KP1,
446 indicating no uptake of these components (Figures S12 and S13). The adsorbed amounts of the
447 weak components were thus determined from the desorption curves. Insignificant uptake was
448 calculated upon blank subtraction, indicating an exceptionally high, virtually infinite selectivity
449 toward CO_2 over the weak components (Table 3). CO_2 exhibited different elution behavior
450 compared to N_2 and CH_4, with breakthrough times varying between the samples. During the
451 adsorption step using the $He/N_2/CO_2$ mixture, CO_2 breakthrough occurred at 10.9 min for KP1,
452 which is 10 times longer than KP2, where CO_2 eluted from the column after only 1.0 min. A
453 similar trend was observed in the adsorption step using the $He/CH_4/CO_2$ mixture, where CO_2
454 breakthrough took place after 9.9 min for the KP1 sample, while for KP2, CO_2 was detected after
455 1.1 min, confirming that KP1 offers much better separation performance for both flue gas and
456 biogas. Meanwhile, the CO_2 breakthrough capacity for $He/N_2/CO_2$ and He/CH4/CO_2 mixtures on
457 KP1 (Table 3) was calculated as 1.33 and 1.23 mmol/g, respectively, which is almost ten times
458 higher than that of KP2 (0.18 and 0.18 mmol/g, respectively). The calculated CO_2 uptake for KP1

closely aligns with the results from the single-component adsorption isotherm (1.50 and 1.56 mmol/g) at 0.05 and 0.10 bar, respectively, at 25 °C, clearly confirming the extremely high selectivity. In contrast, for KP2, the adsorbed amounts in both mixtures were relatively low compared to the single-component adsorption isotherm (1.44 and 1.45 mmol/g). This reduced capacity in KP2 results from a rapid saturation of most favorable adsorption sites, suggesting that CO_2 was predominantly adsorbed on the external surface and in pore openings, likely due to the higher diffusion resistance in larger KP2 crystals. This leads to a discrepancy between the adsorption capacity reported in Table 1 and the breakthrough curve in Figure 7. Under dynamic conditions, the flux gas mixture passes through the sample. Once the most favorable adsorption sites on the external surface of KP2 are fully occupied, CO_2 molecules cannot diffuse and migrate to the internal adsorption sites fast-enough. Consequently, CO_2 starts appearing in the outlet stream (reaching breakthrough). This limitation in diffusion under dynamic conditions leads to a much lower observed CO_2 adsorption capacity for KP2 compared to the static measurements performed at thermodynamical equilibrium only using a pure gas. This is thus referred as the working capacity.

Table 3. Adsorption Capacity of CO_2, N_2 and CH_4, and CO_2/N_2, and CO_2/CH_4 Molar Selectivities for KP2 and KP1 Calculated at Saturation from Breakthrough Curve Analysis at 25 °C.

sample	**CO_2/N_2**			**CO_2/CH_4**		
	capacity (mmol/g)		**selectivity**	**capacity (mmol/g)**		**selectivity**
	CO_2	**N_2**		**CO_2**	**CH_4**	
KP2	0.179	≈ 0	-	0.176	≈ 0	-
KP1	1.332	0.012	555	1.213	0.006	303

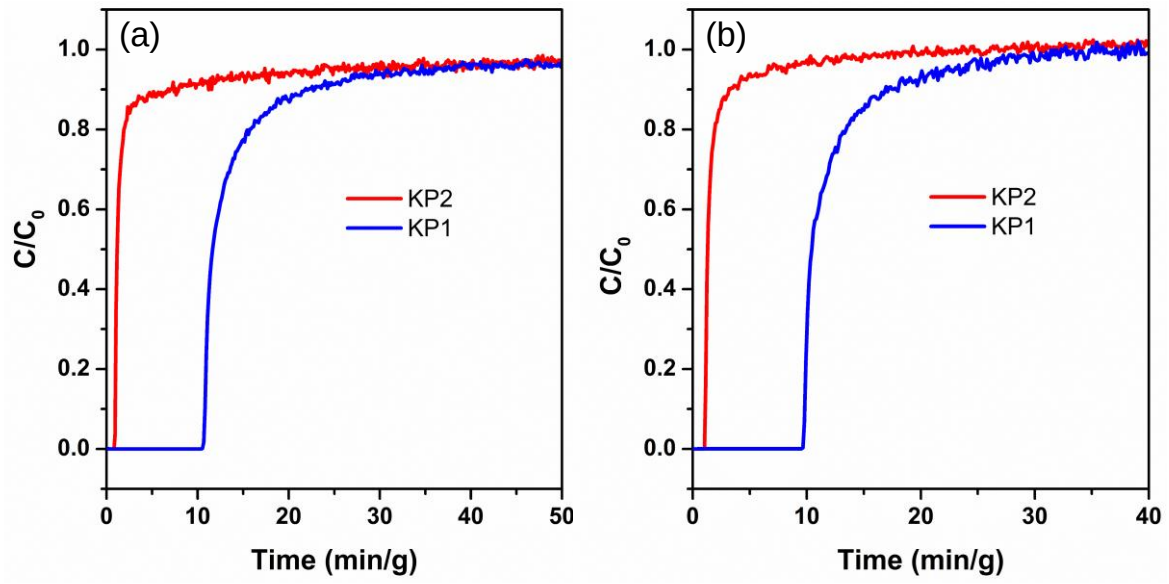

Figure 7: CO_2 breakthrough curves at 25 °C obtained from competitive dynamic adsorption experiments, CO_2/N_2/He, 5/25/70 (a) and CO_2/CH_4/He, 10/15/75 (b).

Once saturation was attained, a desorption step was performed by switching the flow back to a 100% He stream. The results indicated a nice correlation between the desorption behavior and the CO_2 uptake. Specifically, the desorption time was observed to be longer for KP1 as compared to KP2, reflecting the disparity in the adsorbed amounts between the two samples. The shorter adsorption time for KP2 suggests that CO_2 was predominantly adsorbed on the external surface and in pore openings, likely due to the higher diffusion resistance in larger KP2 crystals.

4. Conclusion

In this study, embracing the principles of green chemistry, we have developed a template-free seed-assisted method for zeolite P synthesis. Using pre-synthesized micron-sized zeolite P2 as seeds, the seed-assisted approach yielded highly pure nanocrystalline zeolite P1 with the particle size in the range 30−120 nm, building spherical agglomerates.

K-exchanged P zeolites' CO_2 adsorption and separation performance were investigated under static and dynamic conditions, including a detailed examination of adsorption kinetics under

494 static conditions. Single-component CO_2 adsorption at equilibrium demonstrated higher CO_2
495 uptake and faster adsorption kinetics for nanosized zeolite KP1 compared to the micron-sized
496 zeolite KP_2, with negligible uptake observed for weakly adsorbing components N_2 and CH_4 for
497 both samples. The adsorption kinetics results revealed higher adsorption rates and a more
498 uniform CO_2 diffusion pattern for KP1 compared to KP2. Notably, in KP1, the diffusion
499 mechanism is primarily governed by intra-crystalline diffusion, in contrast to KP2, where
500 diffusion is dominated by surface barrier resistance. Consequently, the distinctive adsorption
501 kinetics observed for the two zeolite samples significantly influenced dynamic adsorption.
502 Breakthrough curve analysis revealed longer breakthrough times, higher CO_2 uptake, and
503 excellent CO_2/N_2 and CO_2/CH_4 selectivities for KP1. Conversely, KP2 exhibited a shorter
504 breakthrough time and very low CO_2 uptake attributed to diffusion limitations. These findings
505 suggest nanosized zeolite KP1 as a promising adsorbent for capturing and separating CO_2 from
506 power-plant flue gas and biogas, particularly under low CO_2 partial pressure conditions.

507 **ASSOCIATED CONTENT**

508 The Supporting Information. Contains information pertaining to Breakthrough curve
509 measurements details, XRD patterns at different temperature and time, SEM and TEM images,
510 ^{27}Al and ^{29}Si NMR spectra, TG analysis, CO_2 adsorption isotherms, the entire competitive
511 dynamic adsorption step, and chemical composition and textural properties details of all samples.

512 **Nomenclature**

513 c_{in} concentration at column inlet, mol m^{-3}

514 c_{out} concentration at column outlet, mol m^{-3}

515 D_e effective diffusivity, $m^2\ s^{-1}$

516 L diffusion length, m

$n_{adsorbed}$	amount of molecules adsorbed, mol
p_i	partial pressure of component i, bar
q_i	equilibrium molar uptake of component i, mmol g^{-1}
Q_{max}	total amount adsorbed at equilibrium, mmol g^{-1}
Q_t	total amount adsorbed after time, mmol g^{-1}
r	radius of the crystallites, m
S_{ads}	adsorption selectivity of the adsorbate
t	time, s
T	temperature, °C
V_{He}	volume of He, m^3
V_{in}	volume at column inlet, m^3
V_{out}	volume at column outlet, m^3
$y_{adsorptive,i}$	adsorptive volume fraction
α	surface permeability, m s^{-3}

AUTHOR INFORMATION

Corresponding Authors

*E-mail : valentin.valtchev@ensicaen.f

*E-mail : remy.guillet-nicolas@ensicaen.fr

Notes

The authors declare no competing financial interest.

Acknowledgments

V. V acknowledges partial financial support from the European Union-NextGenerationEU through the National Recovery and Resilience Plan of the Republic of Bulgaria project No. BG-RRP- 2.004-0008.

References

(1) Bui, M.; Adjiman, C. S.; Bardow, A.; Anthony, E. J.; Boston, A.; Brown, S.; Fennell, P. S.; Fuss, S.; Galindo, A.; Hackett, L. A.; Hallett, J. P.; Herzog, H. J.; Jackson, G.; Kemper, J.; Krevor, S.; Maitland, G. C.; Matuszewski, M.; Metcalfe, I. S.; Petit, C.; Puxty, G.; Reimer, J.; Reiner, D. M.; Rubin, E. S.; Scott, S. A.; Shah, N.; Smit, B.; Trusler, J. P. M.; Webley, P.; Wilcox, J.; Dowell, N. M. Carbon Capture and Storage (CCS): The Way Forward. *Energy Environ. Sci.* **2018**, *11* (5), 1062–1176.

(2) Paltsev, S.; Morris, J.; Kheshgi, H.; Herzog, H. Hard-to-Abate Sectors: The Role of Industrial Carbon Capture and Storage (CCS) in Emission Mitigation. *Appl. Energy* **2021**, *300*, 117322.

(3) Cao, Z.; Anjikar, N. D.; Yang, S. Small-Pore Zeolite Membranes: A Review of Gas Separation Applications and Membrane Preparation. *Separations* **2022**, *9* (2), 47.

(4) Chen, K.; Mousavi, S. H.; Singh, R.; Snurr, R. Q.; Li, G.; Webley, P. A. Gating Effect for Gas Adsorption in Microporous Materials—Mechanisms and Applications. *Chem. Soc. Rev.* **2022**, *51* (3), 1139–1166.

(5) Kerstens, D.; Smeyers, B.; Van Waeyenberg, J.; Zhang, Q.; Yu, J.; Sels, B. F. State of the Art and Perspectives of Hierarchical Zeolites: Practical Overview of Synthesis Methods and Use in Catalysis. *Adv. Mater.* **2020**, *32* (44), 2004690.

(6) Mintova, S.; Gilson, J.-P.; Valtchev, V. Advances in Nanosized Zeolites. *Nanoscale* **2013**, *5* (15), 6693–6703.

(7) Tosheva, L.; Valtchev, V. P. Nanozeolites: Synthesis, Crystallization Mechanism, and Applications. *Chem. Mater.* **2005**, *17* (10), 2494–2513.

(8) Fan, W.; Dong, M. Regulation of Zeolite Particle Morphology. *Science* **2022**, *375* (6576), 29–29.

(9) Pan, T.; Wu, Z.; Yip, A. C. K. Advances in the Green Synthesis of Microporous and Hierarchical Zeolites: A Short Review. *Catalysts* **2019**, *9* (3), 274.

(10) Cao, L.; Hu, Q.; Jin, J.; Xu, C.; Gao, X.; Liu, H.; Lan, L.; Yuan, X.; Liu, H. A Multiple-Assembly/One-Pot-Crystallization Strategy for a Relatively More Eco-Friendly Synthesis of Hydrothermally Stable Mesoporous Aluminosilicates. *RSC Adv.* **2014**, *4* (106), 61631–61633.

(11) Han, Y.; Wu, W.; Li, N.; Yu, X.; Cao, Y.; Xue, M.; Yu, T. Ionothermal Synthesis of Zeotype Materials for Catalysis, Separation and Coatings. *J. Mol. Liq.* **2023**, *386*, 122529.

(12) Zeng, X.; Hu, X.; Song, H.; Xia, G.; Shen, Z.-Y.; Yu, R.; Moskovits, M. Microwave Synthesis of Zeolites and Their Related Applications. *Microporous Mesoporous Mater.* **2021**, *323*, 111262.

(13) Iyoki, K.; Itabashi, K.; Okubo, T. Progress in Seed-Assisted Synthesis of Zeolites without Using Organic Structure-Directing Agents. *Microporous Mesoporous Mater.* **2014**, *189*, 22–30.

(14) Jain, R.; Rimer, J. D. Seed-Assisted Zeolite Synthesis: The Impact of Seeding Conditions and Interzeolite Transformations on Crystal Structure and Morphology. *Microporous Mesoporous Mater.* **2020**, *300*, 110174.

(15) Qin, Z.; Lakiss, L.; Tosheva, L.; Gilson, J.-P.; Vicente, A.; Fernandez, C.; Valtchev, V. Comparative Study of Nano-ZSM-5 Catalysts Synthesized in OH− and F− Media. *Adv. Funct. Mater.* **2014**, *24* (2), 257–264.

(16) Liu, Z.; Wakihara, T.; Oshima, K.; Nishioka, D.; Hotta, Y.; Elangovan, S. P.; Yanaba, Y.; Yoshikawa, T.; Chaikittisilp, W.; Matsuo, T.; Takewaki, T.; Okubo, T. Widening Synthesis Bottlenecks: Realization of Ultrafast and Continuous-Flow Synthesis of High-Silica Zeolite SSZ-13 for NOx Removal. *Angew. Chem.* **2015**, *127* (19), 5775–5779.

(17) Liu, Z.; Zhu, J.; Wakihara, T.; Okubo, T. Ultrafast Synthesis of Zeolites: Breakthrough, Progress and Perspective. *Inorg. Chem. Front.* **2019**, *6* (1), 14–31.

(18) Khalil, U.; Liu, Z.; Peng, C.; Hikichi, N.; Wakihara, T.; García-Martínez, J.; Okubo, T.; Bhattacharya, S. Ultrafast Surfactant-Templating of *BEA Zeolite: An Efficient Catalyst for the Cracking of Polyethylene Pyrolysis Vapours. *Chem. Eng. J.* **2021**, *412*, 128566.

(19) Tang, L.; Haw, K.-G.; He, P.; Fang, Q.; Qiu, S.; Valtchev, V. Synthesis of Zeolite SSZ-24 Using a Catalytic Amount of SSZ-13 Seeds. *Inorg. Chem. Front.* **2019**, *6* (11), 3097–3103.

(20) Grand, J.; Awala, H.; Mintova, S. Mechanism of Zeolites Crystal Growth: New Findings and Open Questions. *CrystEngComm* **2016**, *18* (5), 650–664.

(21) O. Bok, T.; P. Andriako, E.; E. Knyazeva, E.; I. Ivanova, I. Engineering of Zeolite BEA Crystal Size and Morphology via Seed-Directed Steam Assisted Conversion. *RSC Adv.* **2020**, *10* (63), 38505–38514.

(22) Li, Y.; Li, Y.; Yang, Z.; Xu, W.; Gui, T.; Wu, X.; Zhu, M.; Chen, X.; Kita, H. Rapid Synthesis of High-Selective Al-Rich Beta Zeolite Membrane via an Organic Template-Free Route for Pervaporation Dehydration of Water-n-Butanol Mixtures. *Sep. Purif. Technol.* **2023**, *308*, 122969.

(23) Bu, L.; Wang, Y.; Liu, W.; Chu, K.; Guo, N.; Huang, Y.; Qu, L.; Su, X.; Zhang, X.; Li, Y. Green Synthesis of Shaped Nano-ZSM-5 toward More Efficient Methanol-to-Hydrocarbon Conversion. *Appl. Catal. Gen.* **2023**, *665*, 119393.

(24) Baerlocher, C.; McCusker, L. B.; Olson, D. H. GIS - I41/Amd. In *Atlas of Zeolite Framework Types (Sixth Edition)*; Baerlocher, C., McCusker, L. B., Olson, D. H., Eds.; Elsevier Science B.V.: Amsterdam, 2007; pp 146–147.

(25) McCusker, L. B.; Baerlocher, C.; Nawaz, R. Rietveld refinement of the crystal structure of the new zeolite mineral gobbinsite. *Z. Für Krist. - Cryst. Mater.* **1985**, *171* (1–4), 281–290.

(26) Baur, W. H.; Fischer, R. X. *Microporous and Other Framework Materials with Zeolite-Type Structures: Zeolite-Type Crystal Structures and Their Chemistry. 25 New Framework Type Codes and Supplements for Vols. B to G*; Baur, W. H., Fischer, R. X., Eds.; Springer Berlin Heidelberg: Berlin, Heidelberg, 2017.

(27) Oleksiak, M. D.; Ghorbanpour, A.; Conato, M. T.; McGrail, B. P.; Grabow, L. C.; Motkuri, R. K.; Rimer, J. D. Synthesis Strategies for Ultrastable Zeolite GIS Polymorphs as Sorbents for Selective Separations. *Chem. – Eur. J.* **2016**, *22* (45), 16078–16088.

(28) First, E. L.; Hasan, M. M. F.; Floudas, C. A. Discovery of Novel Zeolites for Natural Gas Purification through Combined Material Screening and Process Optimization. *AIChE J.* **2014**, *60* (5), 1767–1785.

(29) Fischer, M.; Bell, R. G. Identifying Promising Zeolite Frameworks for Separation Applications: A Building-Block-Based Approach. *J. Phys. Chem. C* **2013**, *117* (33), 17099–17110.

(30) Dusselier, M.; Davis, M. E. Small-Pore Zeolites: Synthesis and Catalysis. *Chem. Rev.* **2018**, *118* (11), 5265–5329.

(31) Robson, H. *Verified Synthesis of Zeolitic Materials: Second Edition*; Gulf Professional Publishing, 2001.

(32) Kecht, J.; Mihailova, B.; Karaghiosoff, K.; Mintova, S.; Bein, T. Nanosized Gismondine Grown in Colloidal Precursor Solutions. *Langmuir* **2004**, *20* (13), 5271–5276.

(33) Zare, A.; Lashanizadegan, A.; Darvishi, P.; Zerafat, M. M. Synthesis and Characterization of NaP Zeolite Nanocrystals Using [C12mim][Cl] Ionic Liquid. *Chem. Pap.* **2020**, *74* (7), 2163–2174.

(34) Siqueira Oliveira, A. M.; Paris, E. C.; Giraldi, T. R. GIS Zeolite Obtained by the Microwave-Hydrothermal Method: Synthesis and Evaluation of Its Adsorptive Capacity. *Mater. Chem. Phys.* **2021**, *260*, 124142.

(35) Remi, J. C. S.; Lauerer, A.; Chmelik, C.; Vandendael, I.; Terryn, H.; Baron, G. V.; Denayer, J. F. M.; Kärger, J. The Role of Crystal Diversity in Understanding Mass Transfer in Nanoporous Materials. *Nat. Mater.* **2016**, *15* (4), 401–406.

(36) Clatworthy, E. B.; Ghojavand, S.; Guillet-Nicolas, R.; Gilson, J.-P.; Llewellyn, P. L.; Nesterenko, N.; Mintova, S. Dynamic Adsorption of CO_2 by CHA Zeolites – Size Matters. *Chem. Eng. J.* **2023**, *471*, 144557.

(37) Maldonado, M.; Oleksiak, M. D.; Chinta, S.; Rimer, J. D. Controlling Crystal Polymorphism in Organic-Free Synthesis of Na-Zeolites. *J. Am. Chem. Soc.* **2013**, *135* (7), 2641–2652.

(38) Katović, A.; Subotić, B.; Šmit, I.; Despotović, L. A. Crystallization of Tetragonal (B8) and Cubic (B1) Modifications of Zeolite NaP from Freshly Prepared Gel. Part 1. Mechanism of the Crystallization. *Zeolites* **1989**, *9* (1), 45–53.

(39) Katović, A.; Subotić, B.; Šmit, I.; Despotović, L. A. Crystallization of Tetragonal (B8) and Cubic (B1) Modifications of Zeolite NaP from Freshly Prepared Gel: Part 2. Kinetics of Crystallization. *Zeolites* **1990**, *10* (7), 634–641.

(40) Sharma, P.; Yeo, J.; Han, M. H.; Cho, C. H. Knobby Surfaced, Mesoporous, Single-Phase GIS-NaP1 Zeolite Microsphere Synthesis and Characterization for H_2 Gas Adsorption. *J. Mater. Chem. A* **2013**, *1* (7), 2602.

(41) Jain, R.; Mallette, A. J.; Rimer, J. D. Controlling Nucleation Pathways in Zeolite Crystallization: Seeding Conceptual Methodologies for Advanced Materials Design. *J. Am. Chem. Soc.* **2021**, *143* (51), 21446–21460.

(42) Choi, H. J.; Hong, S. B. Effect of Framework Si/Al Ratio on the Mechanism of CO_2 Adsorption on the Small-Pore Zeolite Gismondine. *Chem. Eng. J.* **2022**, *433*, 133800.

(43) Higuchi, Y.; Miyagawa, S.; Tanaka, S. OSDA-Free and Steam-Assisted Synthesis of PHI Type Zeolite Showing a Unique CO_2 Adsorption Behaviour. *CrystEngComm* **2022**, *24* (21), 3859–3864.

(44) Choi, H. J.; Jo, D.; Min, J. G.; Hong, S. B. The Origin of Selective Adsorption of CO_2 on Merlinoite Zeolites. *Angew. Chem. Int. Ed.* **2021**, *60* (8), 4307–4314.

(45) Shang, J.; Li, G.; Singh, R.; Gu, Q.; Nairn, K. M.; Bastow, T. J.; Medhekar, N.; Doherty, C. M.; Hill, A. J.; Liu, J. Z.; Webley, P. A. Discriminative Separation of Gases by a "Molecular Trapdoor" Mechanism in Chabazite Zeolites. *J. Am. Chem. Soc.* **2012**, *134* (46), 19246–19253.

(46) Coudert, F.-X.; Kohen, D. Molecular Insight into CO_2 "Trapdoor" Adsorption in Zeolite Na-RHO. *Chem. Mater.* **2017**, *29* (7), 2724–2730.

(47) Liu, Q.; Mace, A.; Bacsik, Z.; Sun, J.; Laaksonen, A.; Hedin, N. NaKA Sorbents with High CO2-over-N2 Selectivity and High Capacity to Adsorb CO_2. *Chem. Commun.* **2010**, *46* (25), 4502.

(48) Yang, J.; Yuan, N.; Xu, M.; Liu, J.; Li, J.; Deng, S. Enhanced Mass Transfer on Hierarchical Porous Pure Silica Zeolite Used for Gas Separation. *Microporous Mesoporous Mater.* **2018**, *266*, 56–63.

(49) Kim, H.; Cho, H. S.; Kim, C.; Choi, M. Gradual Disordering of LTA Zeolite for Continuous Tuning of the Molecular Sieving Effect. *J. Phys. Chem. C 2017, 121 (12)*, 6807–6812.

(50) Park, Y.; Ju, Y.; Park, D.; Lee, C.-H. Adsorption Equilibria and Kinetics of Six Pure Gases on Pelletized Zeolite 13X up to 1.0 MPa: CO_2 , CO, N_2 , CH_4 , Ar and H_2. *Chem. Eng. J.* **2016**, *292*, 348–365.

(51) Liu, Q.; He, P.; Qian, X.; Fei, Z.; Zhang, Z.; Chen, X.; Tang, J.; Cui, M.; Qiao, X.; Shi, Y. Enhanced CO_2 Adsorption Performance on Hierarchical Porous ZSM-5 Zeolite. Energy Fuels 2017, 31 (12), 13933–13941.

(52) Lee, H.; Shin, J.; Choi, W.; Choi, H. J.; Yang, T.; Zou, X.; Hong, S. B. PST-29: A Missing Member of the RHO Family of Embedded Isoreticular Zeolites. *Chem. Mater.* **2018**, *30* (19), 6619–6623.

(53) Choi, H. J.; Jo, D.; Min, J. G.; Hong, S. B. The Origin of Selective Adsorption of CO_2 on Merlinoite Zeolites. *Angew. Chem. Int. Ed.* **2021**, *60* (8), 4307–4314.

(54) Gong, J.; Wang, C.; Zeng, C.; Zhang, L. Hydrothermal Preparation of Hierarchical SAPO-34 Constructed by Nano-Sheets Using Rapeseed Pollen Extract as Water and Its CO_2 Adsorption Property. *Microporous Mesoporous Mater.* **2016**, *221*, 128–136.

(55) Wang, X.; Yan, N.; Xie, M.; Liu, P.; Bai, P.; Su, H.; Wang, B.; Wang, Y.; Li, L.; Cheng, T.; Guo, P.; Yan, W.; Yu, J. The Inorganic Cation-Tailored "Trapdoor" Effect of Silicoaluminophosphate Zeolite for Highly Selective CO_2 Separation. *Chem. Sci.* **2021**, *12* (25), 8803–8810.

(56) Al Atrach, J.; Golub, I. E.; Clatworthy, E. B.; Rey, J.; Xiong, Y.; Daouli, A.; Desmurs, M.; Badawi, M.; Guillet-Nicolas, R.; Valtchev, V. Mg-Exchanged Gismondine for Superior CO_2/N_2 and CO_2/CH_4 Separations. *Chem. Mater.* **2024**, 36, 3, 1559–1570

(57) Bower, J. K.; Barpaga, D.; Prodinger, S.; Krishna, R.; Schaef, H. T.; McGrail, B. P.; Derewinski, M. A.; Motkuri, R. K. Dynamic Adsorption of CO_2/N_2 on Cation-Exchanged Chabazite SSZ-13: A Breakthrough Analysis. *ACS Appl. Mater. Interfaces* **2018**, *10* (17), 14287–14291.

(58) McEwen, J.; Hayman, J.-D.; Ozgur Yazaydin, A. A Comparative Study of CO_2, CH_4 and N_2 Adsorption in ZIF-8, Zeolite-13X and BPL Activated Carbon. *Chem. Phys.* **2013**, *412*, 72–76.

(59) Hu, Z.; Peng, Y.; Kang, Z.; Qian, Y.; Zhao, D. A Modulated Hydrothermal (MHT) Approach for the Facile Synthesis of UiO-66-Type MOFs. *Inorg. Chem.* **2015**, *54* (10), 4862–4868.

(60) Zhang, X.; Zheng, Q.; He, H. Multicomponent Adsorptive Separation of CO_2, CH_4, N_2, and H_2 over M-MOF-74 and AX-21@M-MOF-74 Composite Adsorbents. *Microporous Mesoporous Mater.* **2022**, *336*, 111899.

(61) Lin, R.-B.; Li, L.; Alsalme, A.; Chen, B. An Ultramicroporous Metal–Organic Framework for Sieving Separation of Carbon Dioxide from Methane. *Small Struct.* **2020**, *1* (3), 2000022.

(62) Zhou, Y.; Li, Y.; Yuan, X.; Hou, G.; Chu, M.; Kang, H.; Qin, W.; Wu, X. Stacked Nano FAU Zeolite as Hierarchical Murray Material for Enhancing CO_2 Diffusion Kinetics. *Sep. Purif. Technol.* **2023**, *325*, 124729.

Graphical abstract